MDPI

Article

Effect of High-Frequency Sea Waves on Wave Period Retrieval from Radar Altimeter and Buoy Data

Xifeng Wang [1,2,*] and Kaoru Ichikawa [3]

[1]   Interdisciplinary Graduate School of Engineering Sciences, Kyushu University, Fukuoka 8168580, Japan
[2]   School of Marine Science and Environment Engineering, Dalian Ocean University, Dalian 116023, China
[3]   Research Institute for Applied Mechanics, Kyushu University, Fukuoka 8168580, Japan;
     ichikawa@riam.kyushu-u.ac.jp
*   Correspondence: wangxf@riam.kyushu-u.ac.jp; Tel.: +80-3995-9505

Abstract: Wave periods estimated from satellite altimetry data behave differently from those calculated from buoy data, especially in low-wind conditions. In this paper, the geometric mean wave period T_a is calculated from buoy data, rather than the commonly used zero-crossing wave period T_z. The geometric mean wave period uses the fourth moment of the wave frequency spectrum and is related to the mean-square slope of the sea surface measured using altimeters. The values of T_a obtained from buoys and altimeters agree well (root mean square difference: 0.2 s) only when the contribution of high-frequency sea waves is estimated by a wavenumber spectral model to complement the buoy data, because a buoy cannot obtain data from waves having wavelengths that are shorter than the characteristic dimension of the buoy.

1. Introduction

As the statistical character parameters describing the sea state, the wave height and period are important in theoretical research on ocean wave generation, developments in coastal and offshore engineering, and other applications. Traditionally, the significant wave height H_s and the zero-crossing wave period T_z are often obtained from sea wave frequency spectra measured by in situ buoys. However, the use of buoys is restricted to primarily coastal regions and, hence, cannot provide information on global ocean wave conditions.

The advent of synthetic aperture radar (SAR) and the space-borne satellite radar altimeter have changed this situation. Synthetic aperture radar is able to provide the two-dimensional surface wave spectra for longer waves and, hence, can only provide swell information [1]. Alternatively, radar altimeters have the capability of estimating H_s and wind speed, in addition to the sea surface height. Moreover, subsequent studies have also indicated the possibility of retrieving T_z from H_s and the backscatter coefficient σ_0, measurements of altimeters, and numerous empirical models have been proposed in the last two decades (e.g., [2–6]). However, these models perform worse in low-wind conditions than in high-wind conditions. In a recent study, a two-piece altimeter wave period model [6] was proposed which is divided according to σ_0, or the wind speed. This model produces root mean square errors for the estimation of T_z of approximately 0.5 s and 0.9 s for high- and low-wind conditions, respectively.

Note, however, that the wave period determined by altimeters' H_s and σ_0 measurements is referred to as the geometric mean wave period T_a, and is defined differently from the zero-crossing wave period T_z, which could cause a systematic discrepancy in the comparisons. Therefore, in the

present study, the geometric mean wave period T_a^B directly calculated from buoy wave spectra is compared with the geometric mean wave period T_a^A calculated from altimeter measurements.

The remainder of the present study is organized as follows. The dataset used in the present study and the definitions of the wave periods are presented in Sections 2 and 3, respectively. In Section 4, the comparison of T_a^B and T_a^A reveals that T_a^B is larger than T_a^A, primarily because buoys missed high-frequency sea waves having wavelengths that are shorter than the characteristic dimension of the buoy. When a wavenumber spectral model is used to obtain the data for high-frequency sea waves, the compensated buoy wave period T_a^{CB} is confirmed to agree well with T_a^A, as described in Section 5. In Section 6, the difference between T_z and T_a and the effects of high-frequency sea waves are further discussed. Finally, a brief summary is presented in Section 7.

2. Dataset

Datasets of co-located buoy/altimeter measurements have always been used in the retrieval of wave periods from altimeter observations. In the present paper, Version "d" AVISO Geophysical Data Records (GDRs) [7] of Jason-2 data from 2008 to 2014 are used. The buoy data were obtained from the US National Data Buoy Center (NDBC) [8], and a total of 30 buoys located in the open ocean (deeper than 1000 m) were chosen in order to avoid shallow water effects (Figure 1). The space and time separation criteria between altimeter and buoy measurements were set to 50 km and 30 min, respectively. The median of the altimeter measurement within 50 km of the buoy recommended by [9] was used to reduce the random sampling variability. After removing some outliers, 4196 pairs of co-located measurements were obtained.
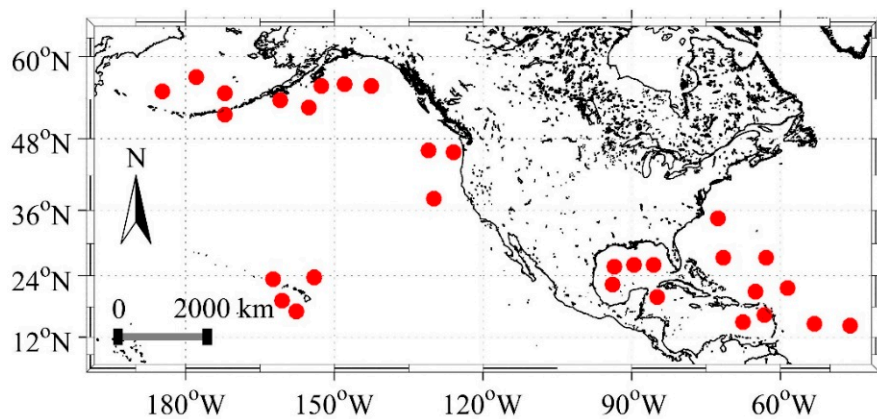

Figure 1. Locations of the 30 collocated National Data Buoy Center (NDBC) buoys.

3. Rationale of the Retrieval of Altimeter Wave Period

A sea state is the condition of the ocean surface, considered as a stochastic field, that is characterized by statistics such as the wave height, period, and direction-independent wavenumber spectrum $\varphi(k)$ or frequency spectrum $F(f)$, where f is the frequency in Hz and k is the wavenumber. In the case of buoy measurements, $F(f)$ is determined through a time series of buoy motion, and all of the basic wave measurements are derived from n-th wave spectral moments, which are defined as:

$$m_n = \int_0^\infty f^n F(f)\, df, \text{ for } n = \ldots, -3, -2, -1, 0, 1, 2, 3, \ldots \tag{1}$$

Based on the linear theory assumption, the basic wave height and period parameters are calculated as follows [10]:

Significant wave height (H_s):

$$H_s = 4\sqrt{m_0} \tag{2}$$

Average zero-crossing wave period (T_z):

$$T_z = \sqrt{\frac{m_0}{m_2}} \tag{3}$$

Moreover, the crest period T_c is defined as follows:

$$T_c = \sqrt{\frac{m_2}{m_4}} \tag{4}$$

A wave buoy, which is finite in size, is not able to follow waves having wavelengths shorter than the approximate diameter of the buoy, and the corresponding limiting frequency is called the cut-off frequency. In the present study, we use f_l and f_u to represent the lower and upper cut-off frequencies, respectively. For most of the NDBC buoys considered in the present study, f_l is 0.02 Hz, since waves with periods longer than 50 s are practically negligible. Meanwhile, f_u is 0.485 Hz, and thus, based on the deep water dispersion relationship, $f^2 = (2\pi)^{-2} gk$, data for high-frequency sea waves having wavelengths of less than approximately 6.6 m are not captured.

Unlike buoy measurements, radar altimeters cannot capture the spectral information of sea waves. Instead, H_s and σ_0 are directly derived from the one-second averaged time series of the sea surface echo of microwave radar (namely the waveform). We hereinafter use superscripts A and B to indicate altimeter and buoy measurements, respectively. For example, H_s^A and H_s^B represent significant wave height measurements obtained by an altimeter and a buoy, respectively.

For near-nadir incidence radar applications, the backscatter coefficient, σ_0, is commonly considered as being due primarily to specular reflection and is inversely proportional to the wind stress. For an isotropic rough surface having a Gaussian distribution, the backscatter coefficient due to specular reflection can be expressed as follows [11]:

$$\sigma_0 = \frac{|R(0)|^2}{MSS^A} \sec^4\theta \exp\left(-\frac{\tan^2\theta}{MSS^A}\right), \tag{5}$$

where σ_0 is the backscatter coefficient in natural units, $|R(0)|^2$ is the Fresnel reflection coefficient at normal incidence characterizing the surface reflectivity, MSS^A is the filtered mean square slope (*MSS*) of the sea surface measured by altimeter, and θ is the radar incidence angle. In the present study, we use $|R(0)|^2 = 0.61$ [12], and MSS^A represents the portion of surface roughness elements having length scales greater than the diffraction limit, 3λ, where λ is the radar wavelength [13], namely greater than 6.6 cm for the 2.2 cm Ku-band radar altimeter. For normal incidence radar altimeters, $\theta = 0$, Equation (5) can be simplified as follows:

$$\sigma_0 = \frac{|R(0)|^2}{MSS^A}. \tag{6}$$

The *MSS* can be obtained by integrating the slope spectrum, $\varphi(k)k^2$, as [14]:

$$MSS = \int_0^\infty \varphi(k)k^2 dk, \tag{7}$$

where $\varphi(k)$ is the direction-independent wavenumber spectrum. Using the deep water dispersion relationship and the Jacobian operator as in [15], the *MSS* can be expressed using the direction-independent frequency spectrum, $F(f)$, as follows [16]:

$$MSS = \int_0^\infty \frac{(2\pi f)^4}{g^2} F(f) df = \frac{16\pi^4}{g^2} m_4, \tag{8}$$

where m_4 is the fourth spectral moment, and g represents the acceleration of gravity.

Based on Equations (3) and (4), the geometric mean wave period T_a can be defined as follows [1]:

$$T_a = \sqrt{T_z \times T_c} = \left(\frac{m_0}{m_4}\right)^{0.25}. \tag{9}$$

For buoy measurements, T_a can be obtained directly from spectral moments by:

$$T_a^B = \left(\frac{m_0^B}{m_4^B}\right)^{0.25}. \tag{10}$$

Based on Equations (2), (6), (8), and (9), T_a can be derived from altimeter measurements by:

$$T_a^A = \left(\frac{m_0^A}{m_4^A}\right)^{0.25} = \frac{\pi}{\sqrt{g\,|R\,(0)|}} \times \left(\sigma_0(H_s^A)^2\right)^{0.25}. \tag{11}$$

Therefore, both altimeter and buoy measurements can be used to obtain T_a. Note that this formulation is very similar to that of [3], which used heuristic arguments to show that the wave period can be retrieved using a linear relationship, namely $T \sim \left(\sigma_0 H_s^2\right)^{0.25}$.

4. Comparison of Geometric Mean Wave Periods Determined from Buoy and Altimeter Data

In this paper, we use various statistics to quantify the comparisons, namely the correlation coefficient (CC), bias, slope of the regression line, and root mean square difference (RMSD) around the regression line. First, the wave periods T_z^B and T_a^A, which are defined differently, are compared, as shown in Figure 2. Referring to the two-piece wave model proposed by [6], the plots are divided according to the wind speed conditions. The geometric mean wave period determined by altimeter data T_a^A is positively correlated with the zero-crossing wave period determined by buoy data T_z^B under all wind conditions. However, as the wind speed decreases, the CC and RMSD around the regression line estimated by the orthogonal distance regression (ODR) method [17] become small and large, respectively, as shown in Table 1. In addition, T_a^A is always significantly shorter than T_z^B. This could be due to either the difference in the definitions of the wave periods or the observation methods, or even due to improper choice of the $|R\,(0)|^2$ constant.
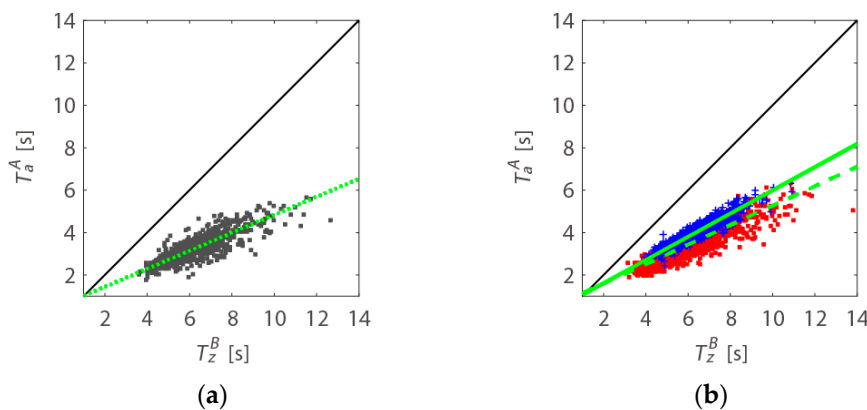

Figure 2. Buoy T_z^B and altimeter T_a^A data when the wind speed is lower (**a**) or higher (**b**) than 5 m·s^{-1}. In the right-hand panel, the blue (red) plots indicate data for which the wind speed is higher (lower) than 10 m·s^{-1}. The regression lines estimated by the orthogonal distance regression (ODR) method are plotted by the dashed (0–5 m·s^{-1}), broken (5–10 m·s^{-1}), and solid (>10 m·s^{-1}) green lines.

Table 1. Correlation coefficient (CC), bias, slope of the regression line, and root mean square difference (RMSD) around the regression line for T_a^A vs. T_z^B and T_a^A vs. T_a^B for various ranges of wind speed. All CC are significant at the 99.9% confidence level.

	Wind Speed (Data Number)	$u \leq 5 \, \text{m·s}^{-1}$ (727)	$5 < u \leq 10 \, \text{m·s}^{-1}$ (2683)	$u > 10 \, \text{m·s}^{-1}$ (786)	Overall (4196)
T_a^A vs. T_z^B	CC	0.83	0.89	0.94	0.84
	bias $(T_z^B - T_a^A)$	3.1 s	2.5 s	2.3 s	2.5 s
	slope	0.42	0.46	0.55	0.48
	RMSD	0.7 s	0.6 s	0.2 s	0.5 s
T_a^A vs. T_a^B	CC	0.82	0.91	0.93	0.85
	bias $(T_a^B - T_a^A)$	2.1 s	1.5 s	1.4 s	1.6 s
	slope	0.62	0.74	0.79	0.74
	RMSD	0.7 s	0.5 s	0.2 s	0.5 s

Next, the geometric mean wave periods of the buoys T_a^B were directly calculated from wave spectra and were compared with T_a^A, as shown in Figure 3. Compared with Figure 2, the estimated wave periods T_a^B and T_a^A (defined similarly) result in better agreement than wave periods T_z^B and T_a^A (defined differently). In particular, the slope of the regression lines becomes closer to unity. Nevertheless, a mean bias of 1.6 s $(T_a^B - T_a^A)$ and an RMSD of 0.5 s around the regression line remain (Table 1).
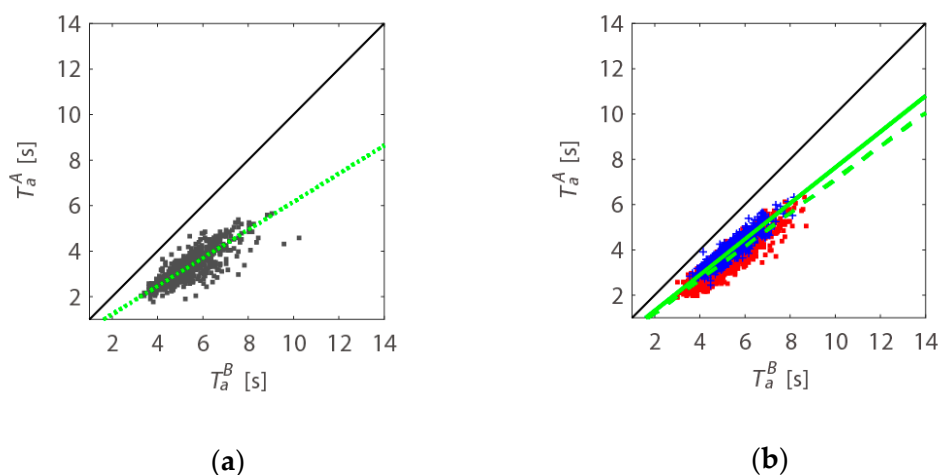

(a)   (b)

Figure 3. Buoy T_a^B and altimeter T_a^A when the wind speed is lower (**a**) or higher (**b**) than $5 \, \text{m·s}^{-1}$. In the right-hand panel, the blue (red) plots indicate data for which the wind speed is higher (lower) than $10 \, \text{m·s}^{-1}$. The regression lines estimated by the ODR method are plotted by the dashed (0–$5 \, \text{m·s}^{-1}$), broken (5–$10 \, \text{m·s}^{-1}$), and solid ($>10 \, \text{m·s}^{-1}$) green lines.

In order to examine the reason for the remaining discrepancy between T_a^A and T_a^B, H_s and *MSS* are examined because they are directly related to m_0 and m_4, respectively, which are used in the derivation of T_a. Altimeters are known for their ability to estimate significant wave height, and this was confirmed by the comparison of the present study, even in low-wind conditions. As shown in Figure 4, the data of altimeter Hs^A almost perfectly agrees with that of buoy Hs^B, as determined by Equation (2), where the CC is 0.98 and the RMSD is 0.2 m.
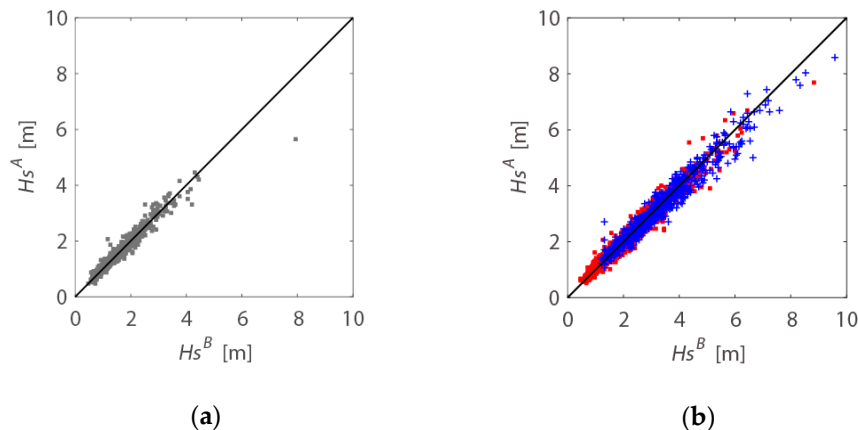
(a)　　　　　　　　　　　　(b)

Figure 4. Buoy H_s^B and altimeter H_s^A when the wind speed is lower (**a**) or higher (**b**) than $5\,\mathrm{m\cdot s^{-1}}$. In the right-hand panel, the blue (red) plots indicate data for the case in which the wind speed is higher (lower) than $10\,\mathrm{m\cdot s^{-1}}$.

On the other hand, the altimeter MSS^A, which is inversely proportional to σ_0, is significantly larger than MSS^B calculated from the fourth moment of the wave spectra, as shown in Figure 5. When the wind speed is higher than $5\,\mathrm{m\cdot s^{-1}}$, MSS^B and MSS^A exhibit a rough linear relationship with the CC exceeding 0.80. In low-wind conditions, the variation range of MSS^B is more limited than that of MSS^A. In other words, MSS^B appears to miss some variations that are observed by the altimeters.

As described in Section 3, the buoy cannot measure waves having wavelengths shorter than the characteristic dimension of the buoy. Such a wave would have a larger slope even though its wave height is small, because its horizontal scale is smaller. Therefore, the high-frequency sea waves not captured by the buoy would contribute significantly to the MSS, as shown in Figure 5, but would contribute less to significant wave height, as shown in Figure 4. In order to confirm this, in the following section, we use a wavenumber spectral model to estimate the MSS of the high-frequency sea waves missed by buoys, and the geometric mean wave period is estimated using the compensated buoy MSS.
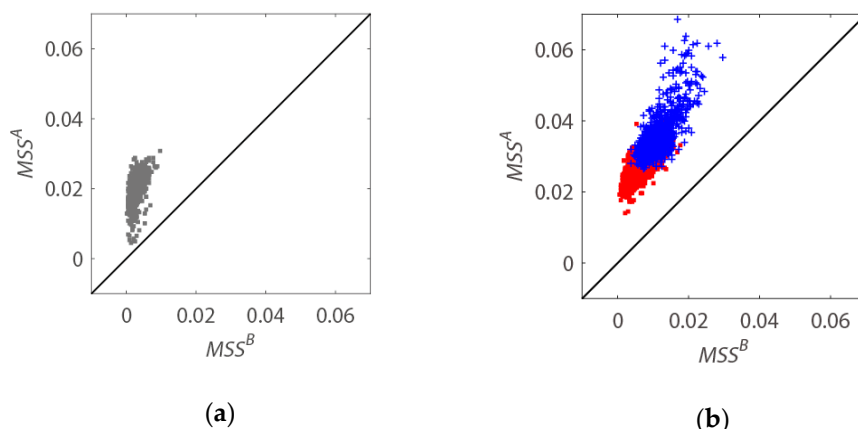

(a)　　　　　　　　　　　　(b)

Figure 5. Buoy MSS^B and altimeter MSS^A when the wind speed is lower (**a**) or higher (**b**) than $5\,\mathrm{m\cdot s^{-1}}$. In the right-hand panel, the blue (red) plots indicate data for the case in which the wind speed is higher (lower) than $10\,\mathrm{m\cdot s^{-1}}$.

5. Compensation of the Mean Square Slope Obtained Using the Buoy Data

As discussed in Section 3, the MSS is theoretically defined by the direction-independent wavenumber spectrum $\varphi(k)$ in Equation (7). Previous studies have shown that the universal form

of the equilibrium range spectrum $\varphi(k) \propto k^{-3}$ is no longer rational and should be of the form $\varphi(k) \propto k^{-2.5}$ [18,19]. Although this form is supported by observations in the rear face region of the spectrum, it cannot be extended to very high wavenumbers. During the last two decades, numerous frequency domain observations have suggested that, in addition to the well-established $k^{-2.5}$ behavior in the rear face region, a fairly abrupt change in spectral slope occurs at approximately $k = 9k_p$, as compared to the slope that follows the k^{-3} law [20], where k_p is the peak wavenumber of wind waves, as defined by $k_p = g/u_{10}{}^2$, and u_{10} is the neutral wind speed at an elevation of 10 m.

Although the proper spectral form remains controversial, the *MSS* of the high-frequency sea waves, MSS^{B-}, is estimated as follows [21]:

$$MSS^{B-} = \int_{k_l}^{k_u} \varphi(k) k^2 dk = \int_{k_l}^{k_1} bu_* g^{-0.5} k^{-0.5} dk + \int_{k_1}^{k_u} Bk^{-1} dk, \tag{12}$$

The first term on the right-hand side of Equation (12) represents the equilibrium range spectrum, and the second term indicates the saturation range spectrum, where $b = 5.2 \times 10^{-2}$, u_* is the wind friction velocity, g is the gravitational acceleration, and $B = 4.6 \times 10^{-2}$. The wavenumbers k_l and k_u reflect the integration limits of the low and high wavenumbers, respectively. Here, $k_l = 0.95$ rad·m^{-1} and $k_u = 100$ rad·m^{-1} are adopted to estimate the *MSS* missing from the buoy measurements, corresponding to wavelengths approximately from 6 cm (or 3λ of Ku-band radar) to 6.6 m (or the characteristic dimension of the buoy). The wavenumber k_1 divides the wavenumber spectrum into the equilibrium range and the saturation range and is defined in [21] as

$$k_1 = \left(\frac{B}{b}\right)^2 \frac{1}{C_d} k_p, \tag{13}$$

where C_d is the drag coefficient for which we adopt the form proposed in [22].

Figure 6 shows the wind speed dependency of MSS^{B-}. As k_p (namely k_1) decreases with the increasing wind speed u_{10}, the first term on the right-hand side of Equation (12) decreases to zero when k_1 becomes smaller than k_l, or when u_{10} exceeds approximately 10 m·s^{-1}.
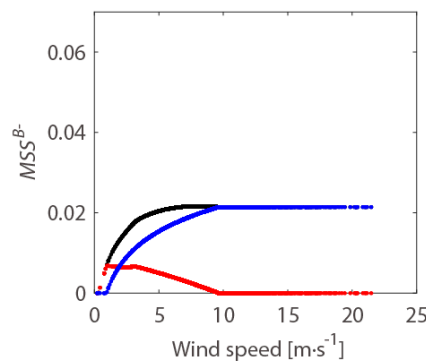

Figure 6. Compensated high-frequency portion of *MSS* for buoys. The red, blue, and black lines represent the equilibrium range, the saturation range, and the total range, respectively.

After compensating for high-frequency sea waves, the compensated buoy mean square slope, $MSS^{CB} = MSS^B + MSS^{B-}$, shows no obvious bias with altimeter MSS^A (Figure 7) compared with the uncompensated buoy mean square slope, MSS^B, even in low-wind conditions. The CC becomes 0.68 and 0.83 for wind speeds lower and higher than 5 m·s^{-1}, respectively.

The geometric mean wave period for the compensated buoy data, T_a^{CB}, was calculated and compared with altimeter-derived T_a^A. As shown in Figure 8, T_a^{CB} is in better agreement with T_a^A than T_a^B (Figure 3). The CC, mean bias ($T_a^{CB} - T_a^A$), and RMSD are 0.97, less than 0.01 s, and 0.2 s, respectively, as listed in Table 2.
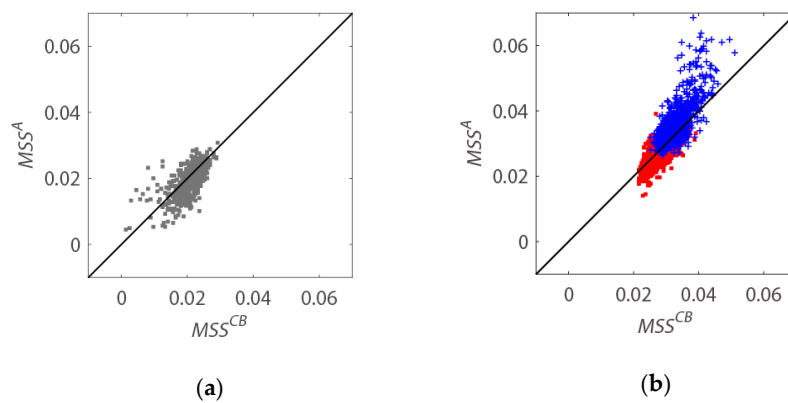
Figure 7. Buoy MSS^{CB} and altimeter MSS^A when the wind speed is lower (**a**) or higher (**b**) than $5\,\mathrm{m\cdot s^{-1}}$. In the right-hand panel, the blue (red) plots indicate data for the case in which the wind speed is higher (lower) than $10\,\mathrm{m\cdot s^{-1}}$.
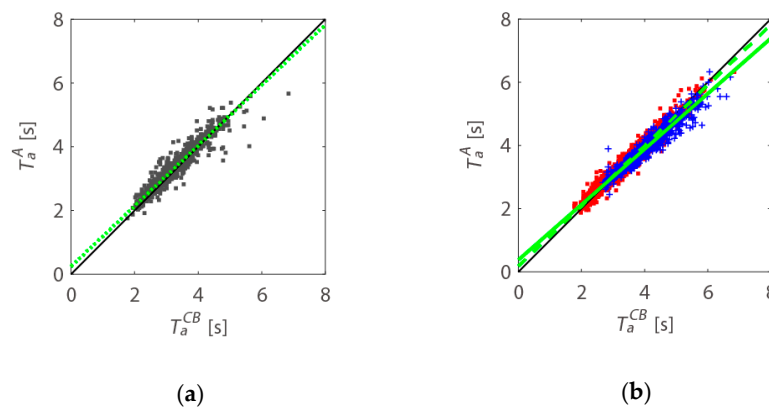

Figure 8. Buoy T_a^{CB} and altimeter T_a^A data when the wind speed is lower (**a**) or higher (**b**) than $5\,\mathrm{m\cdot s^{-1}}$. In the right-hand panel, the blue (red) plots indicate data for which the wind speed is higher (lower) than $10\,\mathrm{m\cdot s^{-1}}$. The regression lines estimated by the ODR method are plotted by the dashed $(0\text{–}5\,\mathrm{m\cdot s^{-1}})$, broken $(5\text{–}10\,\mathrm{m\cdot s^{-1}})$, and solid $(>10\,\mathrm{m\cdot s^{-1}})$ green lines.

Recall that the significant wave height H_s^B is not affected by the loss of high-frequency sea waves, as shown in Figure 4. Since the higher-order moment forces more weight on high-frequency spectra in the integration, the contribution of high-frequency sea waves would become significant for m_4 but negligible for m_0. This suggests that the m_2-based T_z^B would also be affected by the loss of high-frequency sea waves, but in a different manner from the m_4-based T_a^B. Therefore, in the following section, we examine the impact of missing high-frequency sea waves on T_z^B, T_a^B, and T_a^{CB}.

Table 2. Correlation coefficient (CC), bias, slope of the regression line, and root mean square difference (RMSD) around the regression line for T_a^A and T_a^{CB} for various ranges of wind speed. All CC are significant at the 99.9% confidence level.

	Wind Speed (Data Number)	$u \le 5\,\mathrm{m\cdot s^{-1}}$ (727)	$5 < u \le 10\,\mathrm{m\cdot s^{-1}}$ (2683)	$u > 10\,\mathrm{m\cdot s^{-1}}$ (786)	Overall (4196)
	CC	0.94	0.98	0.96	0.97
T_a^A vs. T_a^{CB}	bias $(T_a^{CB} - T_a^A)$	−0.1 s	0.0 s	0.1 s	0.0 s
	slope	0.95	0.95	0.89	0.93
	RMSD	0.2 s	0.1 s	0.2 s	0.2 s

6. Discussion

In order to increase the amount of data for comparison, all data from 30 NDBC buoys are used in this section to calculate T_z^B, T_a^B, and T_a^{CB}, independently from the altimeter data. The data are divided into 16 subsets according to wind speed in intervals of 1 m·s^{-1} (0–1 m·s^{-1}, 1–2 m·s^{-1}, ..., 14–15 m·s^{-1}, and higher than 15 m·s^{-1}). As shown in Figure 9, the data number of each subset exceeds 15,000 with a maximum of approximately 140,000 samples at 6 to 7 m·s^{-1}.
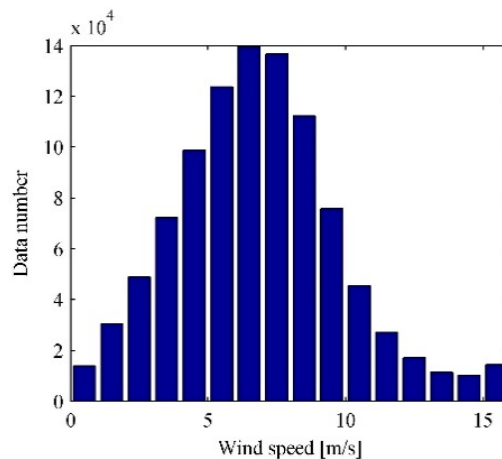

Figure 9. Amount of data for the 16 data subsets.

Figure 10 shows scatter plots of T_z^B with T_a^B or T_a^{CB} for two wind conditions, together with the regression lines estimated by the ODR method. The slopes of the regression lines of T_a^B are closer to unity for both wind conditions. In other words, the discrepancy between T_z^B and T_a^{CB} is much larger. Moreover, the RMSD around the regression line is much larger for T_a^{CB} in the lower wind condition (Figure 10a), whereas, for T_a^B, there is no significant difference between the two wind cases, which suggests that T_a^{CB} is more sensitive to wind speed variation.
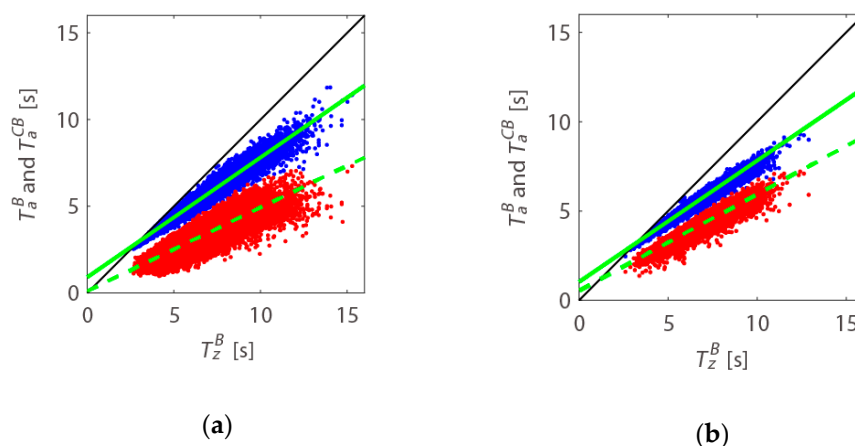

(**a**)

(**b**)

Figure 10. Scatter plot of T_z^B with T_a^B (blue) or T_a^{CB} (red), together with regression lines (solid and broken lines, respectively). For subsets (**a**) wind speed: 4–5 m·s^{-1} and (**b**) wind speed: 10–11 m·s^{-1}.

In order to examine the dependence of the relationship between T_z^B and T_a^B or T_a^{CB} on wind speed, the slope and RMSD of the regression lines were calculated for each of the 16 data subsets, and the results are plotted in Figure 11.
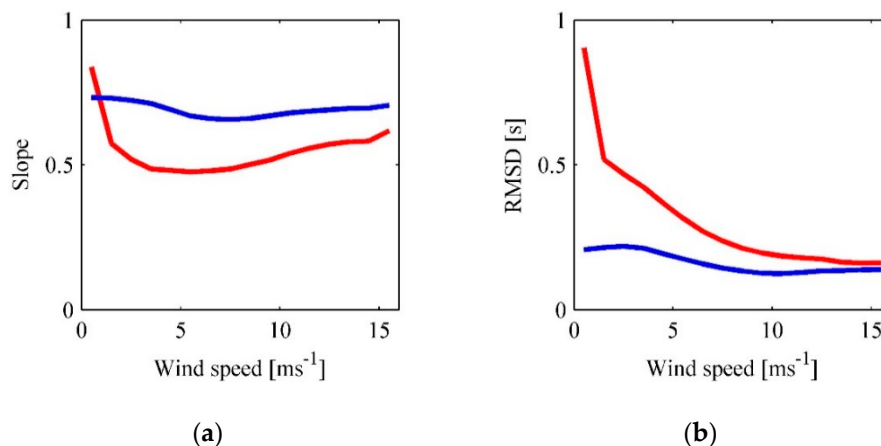
Figure 11. (**a**) Slope of the regression lines of T_a^B (blue) and T_a^{CB} (red) for 16 data subsets; (**b**) RMSD around the regression lines of T_a^B (blue) and T_a^{CB} (red) for 16 data subsets.

For T_a^B, the slope of the regression line varies only slightly with wind speed, and the RMSD remains small. In contrast, for T_a^{CB} (also for T_a^A), the slope of the regression line varies with wind speed, especially in low-wind conditions. The presence of wind waves on background swells shortens T_a^{CB}, resulting in the smaller slope of the regression lines. Since wind waves are more sensitive to wind speeds than swells, the growth of short wind waves decreases the slope values in Figure 11a as the wind speed increases until the wind wave spectrum becomes saturated at winds stronger than 5 m·s^{-1}. On the other hand, neither T_a^B nor T_z^A includes short wind waves, and so they are independent of the growth of short wind waves. Therefore, the slope of T_a^B remains approximately constant, as shown in Figure 11a.

In addition, because the growth of wind waves depends on not only wind speed but also wind duration, the mean wave periods would diverge even for the same instantaneous wind speed, especially for T_a^{CB}, which is most sensitive to the growth of wind waves. This would result in a larger RMSD of T_a^{CB} at a lower wind speed and is consistent with Figure 11b.

7. Conclusions

In previous studies on altimeter wave period retrieval, great efforts were made to establish a relationship between the buoy-derived zero-crossing wave period T_z^B with altimeter-measured significant wave height H_s and the backscatter coefficient σ_0. However, all of the derived algorithms resulted in lower precision in low-wind conditions. Since radar altimeters only provide H_s and σ_0 information about the sea state, that is, the zeroth and fourth wave spectral moments, the geometric mean wave period, $T_a = \left(\frac{m_0}{m_4}\right)^{0.25}$, is estimated from altimeter data and is different from the zero-crossing wave period, $T_z = \left(\frac{m_0}{m_2}\right)^{0.5}$, which is commonly used by in situ buoys. In the present study, the geometric mean wave period T_a^B derived from buoy wave spectra was directly compared with T_a^A.

Higher-order wave spectral moments are more sensitive to high-frequency sea waves. A buoy cannot measure waves shorter than the characteristic dimension of the buoy, so that information of high-frequency sea waves is not captured. Since neither T_z^B nor T_a^B captures the contribution of high-frequency sea waves, they result in a near-linear relationship, independent of wind speed. On the other hand, σ_0 (or the *MSS*) observed by altimeters has high sensitivity to high-frequency sea waves, so that T_a^A is quite different from T_z^B, especially in low-wind conditions.

When the *MSS* due to the missing high-frequency sea waves is compensated, the geometric mean wave period derived from buoy measurements, T_a^{CB}, agrees well with the altimeter-derived period, T_a^A. This suggests that T_a^A observed by altimeters is sufficiently accurate if proper in situ data are compared.

High sensitivity of the *MSS* to high-frequency sea waves is not specific to the radar altimeter measurements, but rather is a common concern with respect to specular reflection. For example, global navigation satellite system reflectometry (GNSS-R) measurements also use the *MSS* at the sea surface, and the retrieved GNSS-R *MSS* was found to be larger than co-located buoy measurements due to the upper cut-off frequency of the buoy [23]. Therefore, the loss of high-frequency waves by buoys should be carefully taken into consideration when buoy measurements are used to verify remote sensing measurements.

Author Contributions: Xifeng Wang contributed to the conception of the study, performed the data analyses, and wrote the manuscript under Kaoru Ichikawa's guidance.

Conflicts of Interest: The authors declare no conflict of interest.

References

1. Collard, F.; Ardhuin, F.; Chapron, B. Extraction of coastal ocean wave fields from SAR images. *IEEE J. Ocean. Eng.* **2005**, *30*, 526–533. [CrossRef]
2. Challenor, P.G.; Srokosz, M.A. Wave studies with radar altimeter. *Int. J. Remote Sens.* **2007**, *12*, 1671–1686. [CrossRef]
3. Gommenginger, C.P.; Srokosz, M.A.; Challenor, P.G.; Cotton, P.D. Measuring ocean wave period with satellite altimeters: A simple empirical model. *Geophys. Res. Lett.* **2003**, *30*. [CrossRef]
4. Quilfen, Y.; Chapron, B.; Serre, M. Calibration/validation of an altimeter wave period model and application to TOPEX/Poseidon and Jason-1 altimeters. *Mar. Geod.* **2004**, *27*, 535–549. [CrossRef]
5. Caires, S.; Sterl, A.; Gommenginger, C.P. Global ocean mean wave period data: Validation and description. *J. Geophys. Res.* **2005**, *110*. [CrossRef]
6. Mackay, E.B.L.; Retzler, C.H.; Challenor, P.G.; Gommenginger, C.P. A parametric model for ocean wave period from Ku band altimeter data. *J. Geophys. Res.* **2008**, *113*. [CrossRef]
7. *OSTM/Jason-2 Products Handbook*; Le site du Centre national d'études spatiales (CNES): Paris, France, 2015.
8. *Nondirectional and Directional Wave Data Analysis Procedures, National Buoy Data Center (NDBC) Technical Document 96-01*; Neptune Sciences Inc.: Slidell, LA, USA, 1996; p. 37.
9. Carter, D.J.T. *Development of Procedures for the Analysis of ERS-1 Radar Altimeter Wind and Wave Data, Using GEOSAT Data*; Study Rep. 8315/89/HE-I; Europe Space Agency: Paris, France, 1990.
10. Tucker, M.J. *Waves in Ocean Engineering: Measurement, Analysis, Interpretation*, 1st ed.; Ellis Horwood Ltd.: Chichester, UK, 1992.
11. Barrick, D. Wind dependence of quasi-specular microwave sea scatter. *IEEE Trans. Antennas Propag.* **1974**, *22*, 135–136. [CrossRef]
12. Klein, L.A.; Swift, C.T. An improved model for the dielectric constant of sea water at microwave frequencies. *IEEE J. Ocean. Eng.* **1977**, *25*, 104–111. [CrossRef]
13. Vendemark, D.; Chapron, B.; Sun, J.; Crescenti, G.H.; Graber, H.C. Ocean wave slope observations using radar backscatter and laser altimeters. *J. Phys Oceanogr.* **2004**, *34*, 2825–2842. [CrossRef]
14. Phillips, O.M. *The Dynamics of the Upper Ocean*, 2nd ed.; Cambridge University Press: Cambridge, UK, 1977.
15. Holthuijsen, L.H. *Waves in Oceanic and Coastal Waters*, 1st ed.; Cambridge University Press: Cambridge, UK, 2007.
16. Li, S.Q.; Zhao, D.L.; Zhou, L.M.; Liu, B. Dependence of mean square slope on wave state and its application in altimeter wind speed retrieval. *Int. J. Remote Sens.* **2013**, *34*, 264–275. [CrossRef]
17. Boggs, P.T.; Rogers, J.E. Orthogonal distance regression. *Contemp. Math* **1990**, *112*, 183–194.
18. Phillips, D.M. Effects of the wavenumber spectrum of a sea surface on Laser Beam Reflection. *Aust. J. Phys.* **1979**, *32*, 469–489. [CrossRef]
19. Phillips, O.M. Spectral and statistical properties of the equilibrium range in wind-generated gravity waves. *J. Fluid. Mech.* **1985**, *156*, 505–531. [CrossRef]

20. Hwang, P.A.; Wang, D.W.; Walsh, E.J.; Krabill, W.B.; Swift, R.N. Airborne measurements of the wavenumber spectra of ocean surface waves. Part I: Spectral slope and dimensionless spectral coefficient. *J. Phys. Oceanogr.* **2000**, *30*, 2753–2767. [CrossRef]
21. Hwang, P.A.; Wang, D.W. Directional distributions and mean square slopes in the equilibrium and saturation ranges of the wave spectrum. *J. Phys. Oceanogr.* **2001**, *31*, 1346–1360. [CrossRef]
22. Wu, J. Wind-stress coefficients at light winds. *J. Atmos. Ocean. Technol.* **2009**, *5*, 885–888. [CrossRef]
23. Clarizia, M.P. Investigating the Effect of Ocean Waves on GNSS-R Microwave Remote Sensing Measurement. Ph.D. Thesis, University of Southampton, Southampton, UK, 2012.